RESEARCH ARTICLE

MAGNETISM

Blowing magnetic skyrmion bubbles

Wanjun Jiang,[1] Pramey Upadhyaya,[2] Wei Zhang,[1] Guoqiang Yu,[2] M. Benjamin Jungfleisch,[1] Frank Y. Fradin,[1] John E. Pearson,[1] Yaroslav Tserkovnyak,[3] Kang L. Wang,[2] Olle Heinonen,[1,4,5,6] Suzanne G. E. te Velthuis,[1] Axel Hoffmann[1]*

The formation of soap bubbles from thin films is accompanied by topological transitions. Here we show how a magnetic topological structure, a skyrmion bubble, can be generated in a solid-state system in a similar manner. Using an inhomogeneous in-plane current in a system with broken inversion symmetry, we experimentally "blow" magnetic skyrmion bubbles from a geometrical constriction. The presence of a spatially divergent spin-orbit torque gives rise to instabilities of the magnetic domain structures that are reminiscent of Rayleigh-Plateau instabilities in fluid flows. We determine a phase diagram for skyrmion formation and reveal the efficient manipulation of these dynamically created skyrmions, including depinning and motion. The demonstrated current-driven transformation from stripe domains to magnetic skyrmion bubbles could lead to progress in skyrmion-based spintronics.

Magnetic skyrmions are topological spin textures that can be stabilized by Dzyaloshinskii-Moriya interactions (DMIs) (*1*–*9*) in chiral bulk magnets such as MnSi, FeGe, etc. Owing to their distinct vortex-like spin texture, skyrmions exhibit many fascinating features, including emergent electromagnetic fields, which enable their efficient manipulation (*4*, *5*, *8*–*10*). A particularly technologically interesting property is that skyrmions can be driven by a spin-transfer torque mechanism at a very low current density, which has been demonstrated at cryogenic temperatures (*4*, *5*, *8*, *10*). Besides bulk chiral magnetic interactions, the interfacial symmetry breaking in heavy metal/ultrathin ferromagnet/insulator (HM/F/I) trilayers introduces an interfacial DMI (*11*–*14*) between neighboring atomic spins, which stabilizes Néel walls (cycloidal rotation of the magnetization direction) with a fixed chirality over the Bloch walls (spiral rotation of the magnetization direction) (*15*–*20*). This is expected to result in the formation of skyrmions with a "hedgehog" configuration (*14*, *18*, *21*–*25*). This commonly accessible material system exhibits spin Hall effects from heavy metals with strong spin-orbit interactions (*26*), which in turn give rise to well-defined spin-orbit torques (SOTs) (*17*, *19*, *27*–*29*) that can control magnetization dynamics efficiently. However, it has been experimentally challenging to use the electric current and/or its induced SOTs (*8*, *21*, *23*, *24*, *27*, *30*–*32*) for dynamically creating and/or manipulating hedgehog skyrmions. Here we address that issue.

[1]Materials Science Division, Argonne National Laboratory, Lemont, IL 60439, USA. [2]Device Research Laboratory, Department of Electrical Engineering, University of California, Los Angeles, CA 90095, USA. [3]Department of Physics and Astronomy, University of California, Los Angeles, CA 90095, USA. [4]Department of Physics and Astronomy, Northwestern University, Evanston, IL 60208, USA. [5]Northwestern-Argonne Institute of Science and Engineering, Northwestern University, Evanston, IL 60208, USA. [6]Computation Institute, University of Chicago, Chicago, IL 60637, USA.
*Corresponding author. E-mail: hoffmann@anl.gov

Central to this work is how electric currents can manipulate a chiral magnetic domain wall (DW); that is, the chirality of the magnetization rotation (as shown in Fig. 1A) is identical for every DW. This fixed chirality is stabilized by the interfacial DMI (*17*–*19*, *21*, *28*). In HM/F/I heterostructures, the current flowing through the heavy metal generates a transverse vertical spin current attributable to the spin Hall effect (*27*), which results in spin accumulation at the interface with the ferromagnetic layer. This spin accumulation gives rise to a SOT acting on the chiral DW (Fig. 1A). The resultant effective spin Hall field can be expressed as (*17*–*19*, *27*)

$$\vec{\mathbf{B}}_{\mathrm{sh}} = B_{\mathrm{sh}}^{0}[\hat{m} \times (\hat{z} \times \hat{j}_{\mathrm{e}})] \qquad (1)$$

where $\hat{m}$ is the magnetization unit vector, $\hat{z}$ is the unit vector normal to the film plane, and $\hat{j}_{\mathrm{e}}$ is the direction of electron particle flux. Here B_{sh}^{0} can be written as $(\hbar/2|e|) \cdot (\theta_{\mathrm{sh}} J_{\mathrm{c}}/t_{\mathrm{f}} M_{\mathrm{s}})$, where $\hbar/2$ is the spin of an electron (and $\hbar$ is Planck's constant h divided by 2π), e is the charge of an electron, t_{f} is the thickness of the ferromagnetic layer, and M_{s} is the saturation (volume) magnetization. The spin Hall angle $\theta_{\mathrm{sh}} = J_{\mathrm{s}}/J_{\mathrm{c}}$ is defined by the ratio between spin current density (J_{s}) and charge current density (J_{c}). For homogeneous current flow along the x axis (Fig. 1B), a chiral SOT enables efficient DW motion (*17*–*19*). In the case of a stripe domain with a chiral DW (Fig. 1B), the symmetry of Eq. 1 leads to a vanishing torque on the side walls parallel to the current, and therefore only the end of the stripe domain is moved. If the opposite end is pinned, this results in an elongation of the stripe.

The situation becomes more complex when the stripe domain is subjected to an inhomogeneous current flow. This can be achieved by introducing a geometrical constriction into a current-carrying trilayer wire (Fig. 1C). Such a constriction results in an additional current component along the y axis: j_y around the narrow neck (Fig. 1D). The total current j is spatially convergent (or divergent) to

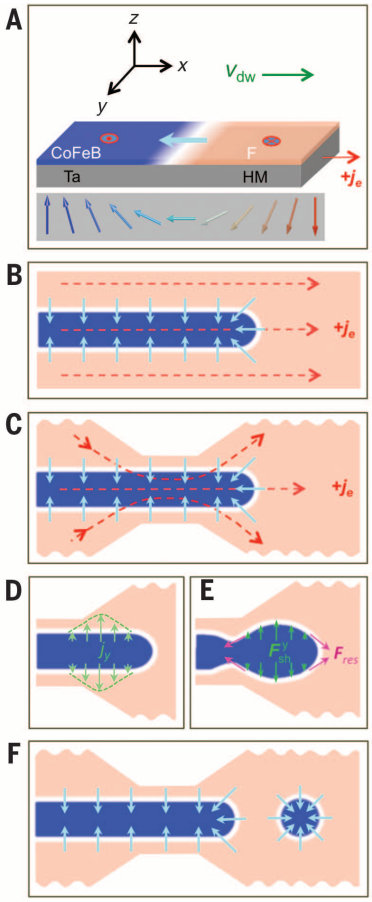

Fig. 1. Schematic of the transformation of stripe domains into magnetic skyrmion bubbles. (**A**) Infinitesimal section of a chiral DW in a ferromagnet (F)/heavy metal (HM) bilayer illustrating the relation between local magnetization vectors and the SOT-induced chiral DW motion of velocity V_{dw} in a device with a homogeneous electron current flow j_e along the +x axis. Blue corresponds to upward orientation of magnetization, whereas orange represents the downward orientation of magnetization. The bottom panel illustrates the magnetization directions inside of the Néel wall. (**B**) Top view of a trilayer device. The blue region is a stripe-shaped domain. Light blue arrows show the in-plane magnetization direction of the DW [as shown in the bottom panel of (A)] and indicate that the domain has left-handed chirality. The red arrows correspond to the current distribution. (**C**) Introducing a geometrical constriction into the device gives rise to an inhomogeneous current distribution, which generates a flow along the y axis (j_y) around the narrow neck. This current distribution is spatially divergent to the right and convergent to the left of the constriction. The y component of the current distribution is highlighted in (**D**). This introduces an effective spin Hall force ($\mathbf{F}^{y}_{sh}$) along the y axis that (**E**) locally expands the stripe domain on the right side. (**F**) Once the expansion approaches a critical point, the resultant restoring forces ($\boldsymbol{F}_{\mathrm{res}}$) associated with the surface tension of the DWs are no longer able to maintain the shape, and the stripe domains break into circular bubble domains, resulting in the formation of synthetic Néel skyrmions.

the left (or right) of the constriction (*33*). Consequently, inhomogeneous effective forces ($\mathbf{F}_{sh}^{y}$) on the DWs (caused by the spin Hall field) are created along the y axis; these forces act to expand the end of the domain (Fig. 1E). As the domain end continually expands its radius, the surface tension in the DW (resulting from the increasing DW energy determined by the combination of exchange and anisotropy fields) increases (*34*), which results in breaking the stripes into circular domains (Fig. 1F).

This process resembles how soap bubbles develop out of soap films upon blowing air through a straw, or how liquid droplets form in fluid flow jets (*35*). Because of the interfacial DMI in the present system, the spin structures of the newly formed circular domains maintain a well-defined (left-handed) chirality (*13*, *14*, *23*, *24*). Once formed, these created synthetic hedgehog (Néel) skyrmions (*14*, *23*) are stable due to topological protection and move very efficiently following the current direction, a process that can be described on the basis of a modified Thiele equation (*36*). The dynamic skyrmion conversion could, in principle, happen at the other side of the device, where the spatially convergent current compresses stripe domains. However, sizeable currents and SOTs are required to compensate the enhanced (repulsive) dipolar interaction. The proposed mechanism differs from a recent theoretical proposal with similar geometry, in which skyrmions are formed from the coalescence of two independent DWs extending over the full width of a narrow constriction at a current density ≈10^8 A/cm^2 (*32*). For repeated skyrmion generation, this latter mechanism requires a continuous generation of paired DWs in the constriction, which is inconsistent with the experimental observations described below.

Transforming chiral stripe domains into skyrmions

We demonstrated this idea experimentally with a Ta(5 nm)/$Co_{20}Fe_{60}B_{20}$(CoFeB)(1.1 nm)/TaO_x(3 nm) trilayer grown by magnetron sputtering (*37*, *38*) and patterned into constricted wires via photolithography and ion milling (*33*). The wires have a width of 60 μm with a 3-μm-wide and 20-μm-long geometrical constriction in the center. Our devices are symmetrically designed across the narrow neck to maintain balanced demagnetization energy. A polar magneto-optical Kerr effect (MOKE) microscope in a differential mode (*39*) was used for dynamic imaging experiments at room temperature. Before applying a current, the sample was first saturated at positive magnetic fields and subsequently a perpendicular magnetic field of $B_\perp = +0.5$ mT was applied; sparse magnetic stripe and bubble domains prevail at both sides of the wire (Fig. 2A). The lighter area corresponds to positive perpendicular magnetization orientation, and the darker area corresponds to negative orientation, respectively.

In contrast to the initial magnetic domain configuration, after passing a 1-s single pulse of current density j_e = +5 × 10^5 A/cm^2 (normalized by the width of the device: 60 μm), it is observed that the stripe domains started to migrate, subsequently forming extended stripe domains on the left side. These domains were mostly aligned with the charge current flow and converged at the left side of constriction. The stripes were transformed into skyrmion bubbles immediately after passing through the constriction (Fig. 2B). These dynamically created skyrmions, varying in size between 700 nm and 2 μm (depending on the strength of the external magnetic field), are stable and do not decay on the scale of a typical laboratory testing period (at least 8 hours). The size of the skyrmions is determined by the interplay between Zeeman, magnetostatic interaction and interfacial DMI. In the presence of a constant electron current density of j_e = +5 × 10^5 A/cm^2, these skyrmions are created with a high speed close to the central constriction and destroyed at the end of the wire. Capturing the transformation dynamics of skyrmions from stripe domains is beyond the temporal resolution of the present setup. Reproducible generation of skyrmions is demonstrated by repeating pulsed experiments several times (*33*). The left side of the device remains mainly in the labyrinthine stripe domain state after removing the pulse current, which indicates that both skyrmion bubbles and stripe domains are metastable.

When the polarity of the charge current is reversed to j_e = −5 × 10^5 A/cm^2, the skyrmions are formed at the left side of the device (Fig. 2, C and D). This directional dependence indicates that the spatially divergent current and SOT, determined by the geometry of the device, are most likely responsible for slicing stripe DWs into magnetic skyrmion bubbles, qualitatively consistent with the schematic presented in Fig. 1.

At a negative magnetic field $B_\perp = -0.5$ mT and current j_e = +5 × 10^5 A/cm^2 (Fig. 2, E and F), a reversed contrast, resulting from opposite inner and outer magnetization orientations, is observed compared with positive fields. We varied the external magnetic field and charge current density systematically and determined the phase diagram for skyrmion formation shown in Fig. 2G. A large population of synthetic skyrmions is found only in the shadowed region, whereas in the rest of phase diagram the initial domain configurations remain either stationary or flowing smoothly, depending on the strength of current density, as discussed below. This phase diagram is independent of pulse duration for pulses longer than 1 μs. No creation of skyrmions in a regular-shaped device with a homogeneous current flow (as illustrated in Fig. 1B) is observed up to a current density of j_e = +5 × 10^6 A/cm^2.

Capturing the transformational dynamics

The conversion from chiral stripe domains into magnetic skyrmions can be captured by decreasing the driving current, which slows down the transformational dynamics. Figure 3, A to D, shows the dynamics for a constant current density of j_e = +6.4 × 10^4 A/cm^2 at $B_\perp = +0.46$ mT. The original (disordered) labyrinthine domains on the left side squeeze to pass through the constriction (Fig.

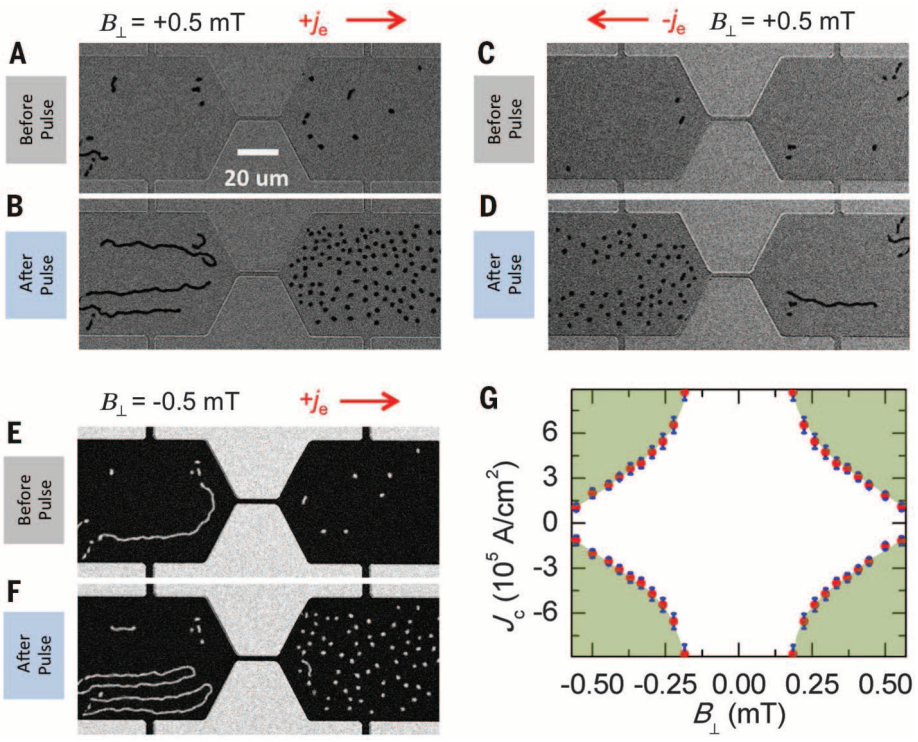

Fig. 2. Experimental generation of magnetic skyrmions. (**A**) Sparse irregular domain structures are observed at both sides of the device at a perpendicular magnetic field of $B_\perp = +0.5$ mT. (**B**) Upon passing a current of j_e = +5 × 10^5 A/cm^2 through the device, the left side of the device develops predominantly elongated stripe domains, whereas the right side converts into dense skyrmion bubbles. (**C** and **D**) By reversing the current direction to j_e = −5 × 10^5 A/cm^2, the dynamically created skyrmions are forming at the left side of the device. (**E** and **F**) Changing the polarity of the external magnetic field reverses the internal and external magnetization of these skyrmions. (**G**) Phase diagram for skyrmion formation. The shaded area indicates field-current combinations that result in the persistent generation of skyrmions after each current pulse.

3B). The stripe domains become unstable after passing through the constriction and are eventually converted into skyrmions on the right side of the device, as shown in Fig. 3, C and D. This can be seen in more detail in the supplementary MOKE movies (movies S1 and S2). Because the x component of the current results in an efficient motion of DWs, the skyrmion formation can occur away from the constriction. The synthetic skyrmions do not merge into stripe domains and, in fact, repel each other, indicating their topological protection as well as magnetostatic interactions.

Some important features should be noticed. There exists a threshold current $j_{e\text{-}sk} = \pm 6 \times 10^4$ A/cm^2 for persistently generating skyrmion bubbles from stripe domains for pulses longer than 1 μs. Above this current, the enhanced spin-orbit torques produce the instability of the DWs, which results in the continuous formation of skyrmions. The present geometry for skyrmion generation is very efficient, resulting in the observed threshold current that is three orders of magnitude smaller than suggested by previous simulation studies (10^7 to 10^8 A/cm^2) in MnSi thin films with a bulk DMI where the driving mechanism is the conventional spin-transfer torque (*30*). Below this threshold for continuous skyrmion generation, there is a threshold depinning current $j_{e\text{-}st} = \pm 4.1 \times 10^4$ A/cm^2 that produces a steady motion of stripe domains. The force (pressure) on the stripe from SOT at this current exceeds the one required to maintain its shape. When $j_{e\text{-}st} < j_e < j_{e\text{-}sk}$, the stripe domains are moving smoothly through the constriction and prevail at both sides of devices, with just the occasional formation of skyrmions.

Depinning and motion of synthesized $S = 1$ skyrmions

The magnetic skyrmion bubbles discussed so far have a topological charge given by the skyrmion number $S = 1$, as is determined by wrapping the unit magnetization vector ($\mathbf{m}$) over the sphere $S = {}^1/_{4\pi}\int \mathbf{m} \cdot (\partial_x \mathbf{m} \times \partial_y \mathbf{m}) dxdy$ (*1*, *8*). These $S = 1$ synthetic skyrmions move because of the opposite direction of effective SOTs on the opposite sides of the skyrmion (Fig. 3E). Following the initialization by a current pulse $j_e = +5 \times 10^5$ A/cm^2 (which is larger than the threshold current $j_{e\text{-}sk}$ for generating skyrmions), we studied the efficient depinning and motion of synthetic skyrmions (Fig. 3, F to I) at $B_\perp = -0.5$ mT. At the current density $j_e = +3 \times 10^4$ A/cm^2, there is no migration of stripe domains through the constriction (hence an absence of newly formed skyrmions). However, it is clear that the previously generated skyrmions at the right side of the device are gradually moving away following the electron flow direction. During the motion, no measurable distortion of these synthetic skyrmions is observed within the experimental resolution, consistent with the well-defined chirality of the skyrmion bubble. The average velocity ($\bar{v} = \ell/\Delta t$) is determined by dividing the displacement (ℓ) with the total time period (Δt). For the present current density, the motion of synthetic skyrmion is stochastic and influenced by random pinning with an average velocity of ≈10 μm/s, the current dependence of which is summarized in Fig. 3J. The ratio of the velocity to the applied current is comparable to what is observed for the chiral DW motion in the related systems (*17*, *19*).

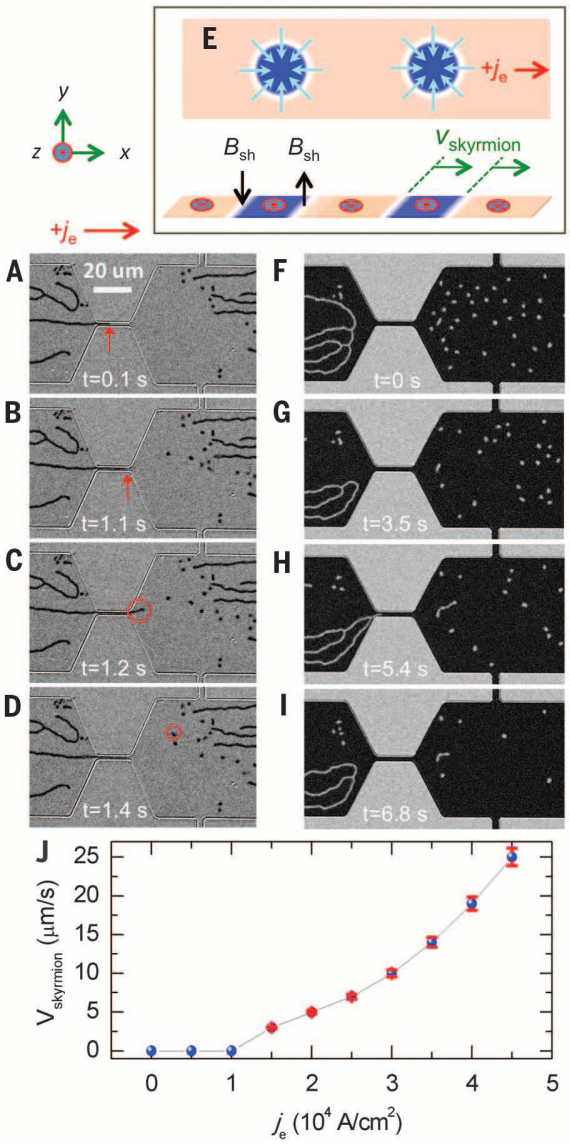

Fig. 3. Capturing the transformational dynamics from stripe domains to skyrmions and motion of skyrmions. (**A** to **D**) At a constant current density $j_e = +6.4 \times 10^4$ A/cm^2 and $B_\perp = +0.46$ mT, the disordered stripe domains are forced to pass through the constriction and are eventually converted into skyrmions at the right side of the device. Red circles highlight the resultant newly formed skyrmions. (**E**) Illustration of the effective spin Hall field acting on these dynamically created skyrmions; the direction of motion follows the electron current. (**F** to **I**) Efficient motion of these skyrmions for a current density $j_e = +3 \times 10^4$ A/cm^2. (F) First, a 1-s-long single pulse $j_e = +5 \times 10^5$ A/cm^2 initializes the skyrmion state. (G to I) Subsequently, smaller currents (below the threshold current to avoid generating additional skyrmions through the constriction) are used to probe the current-velocity relation. These skyrmions are migrating stochastically and moving out of the field of view. See supplementary MOKE movies S1, S2, and S4 for the corresponding temporal dynamics. (**J**) The current-velocity dependence of skyrmions is acquired by studying ≈20 skyrmions via averaging their velocities by dividing the total displacement with the total time period.

Current characteristics of $S = 0$ magnetic bubbles

Because of the competition between long-range dipolar and short-range exchange interaction, a system with a weak perpendicular magnetic anisotropy undergoes a spin reorientation transition with in-plane magnetic fields that is typified by a stripe-to-bubble domain phase transition (*39*, *40*). Such an in-plane field–induced bubble state is established by sweeping the magnetic field from $B_{||} = +100$ to $+10$ mT. Current-driven characteristics of the in-plane field–induced magnetic bubbles are in stark contrast to the mobile magnetic skyrmions generated from SOTs. These bubbles shrink and vanish in the presence of a positive electron current density (Fig. 4, A to E) or elongate and transform into stripe domains in the presence of negative electron current density (Fig. 4, F to J). Such a distinct difference directly indicates the different spin structures surrounding these field-induced bubbles and, therefore, the different skyrmion numbers.

For the in-plane field–induced magnetic bubbles, because the spin structures of DWs follow the external magnetic fields (*18*, *41*, *42*) (Fig. 4K), the corresponding skyrmion number is $S = 0$. Because of the same direction of the effective spin Hall fields given by the reversed DW orientations, topologically trivial $S = 0$ magnetic bubbles experience opposite forces on the DWs at opposite ends. This leads to either a shrinking or elongation of the bubbles, depending on the direction of currents, which is consistent with our experimental observation. This also explains the in-plane current–induced perpendicular magnetization switching in the presence of in-plane fields (*27*, *42*).

Perspectives

Recent experimental efforts toward creating individual magnetic skyrmions use either tunneling current from a low-temperature spin-polarized scanning tunneling microscope (*43*) or geometrical confinement via sophisticated nanopatterning

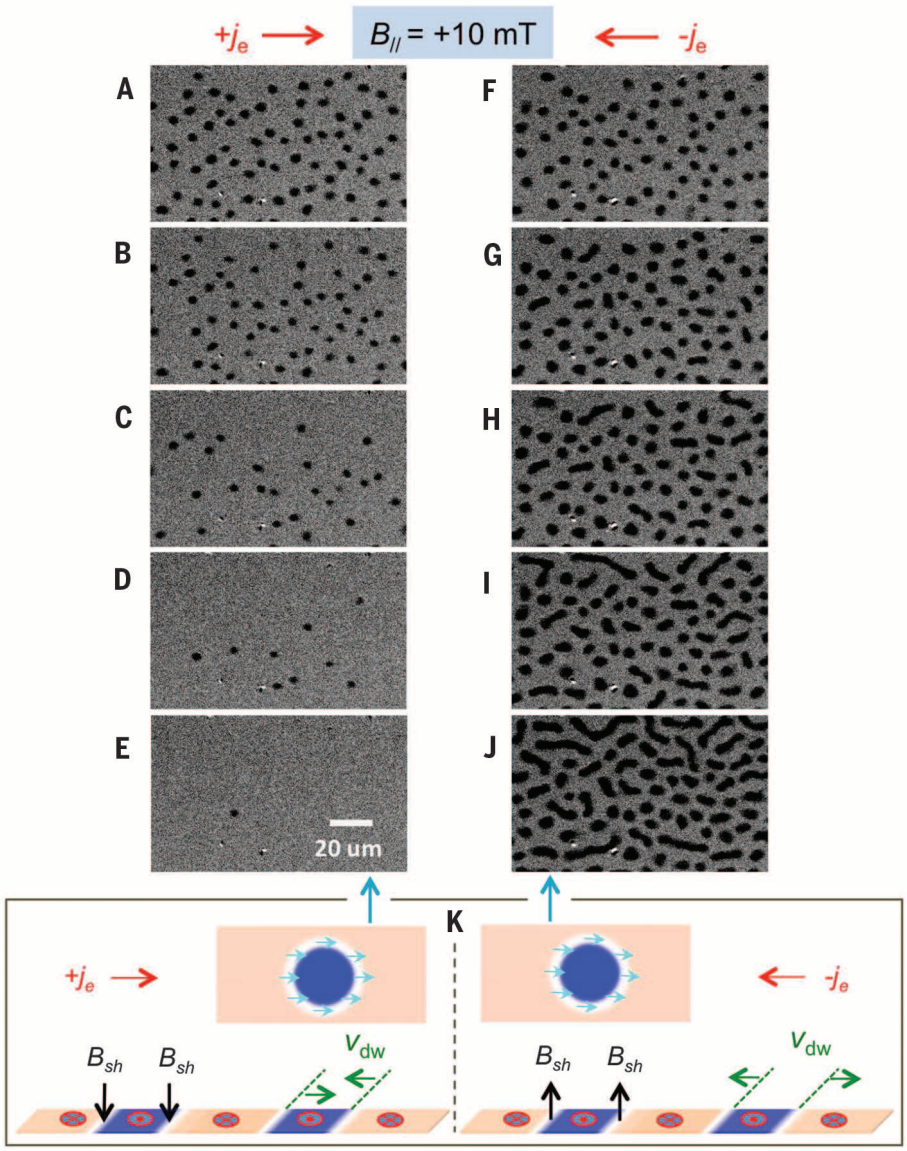

Fig. 4. Absence of motion for the in-plane magnetic fields stabilized *S* = 0 magnetic bubbles. (**A** to **E**) (A) In-plane magnetic field–induced bubbles are created by first saturating at in-plane field $B_{\parallel} = +100$ mT and subsequently decreasing to $B_{\parallel} = +10$ mT. Depending on the direction of the current, these magnetic bubbles either shrink or expand. (A to E) Shrinking bubbles are observed upon increasing the current density from $j_e = +5 \times 10^4$ to $+2.5 \times 10^5$ A/cm^2 in steps of 5×10^4 A/cm^2. (**F** to **J**) Expansion of bubbles is revealed for currents from $j_e = -0.5 \times 10^5$ to -2.5×10^5 A/cm^2 in steps of 5×10^4 A/cm^2. (**K**) These results are linked to the different spin textures (namely, $S = 0$ skyrmion bubbles) that were stabilized along the DW by the in-plane magnetic fields, which lead to different orientations of the effective spin Hall fields and different directions of DW motion, as illustrated.

(*44*–*46*). Our results demonstrate that spatially divergent current-induced SOTs can be an effective way for dynamically generating mobile magnetic skyrmions at room temperature in commonly accessible material systems. The size of these synthetic skyrmions could be scaled down by properly engineering the material-specific parameters that control the various competing interactions in magnetic nanostructures (*23*, *24*, *47*). We expect that similar instabilities will be generated from divergent charge current flows. Whereas the mechanism for synthetic skyrmion generation can be qualitatively linked to the spatially divergent spin Hall spin torque, a comprehensive understanding of this dynamical conversion, particularly at the picosecond or nanosecond time scale where the intriguing magnetization dynamics occurs, requires further experimental and theoretical investigations. Spatially divergent SOT-driven structures also offer a readily accessible model system for studying topological transitions and complex flow instabilities (*35*), where the parameters governing the flow, such as surface tension, can be systematically tuned by the magnetic interactions. At the same time, this dynamic approach for skyrmion generation in the near future could enable the demonstration of advanced skyrmionic device concepts; for example, functional skyrmion racetrack memory (*14*, *23*, *36*, *48*).

REFERENCES AND NOTES

1. U. K. Rößler, A. N. Bogdanov, C. Pfleiderer, *Nature* **442**, 797–801 (2006).
2. S. Mühlbauer *et al.*, *Science* **323**, 915–919 (2009).
3. X. Z. Yu *et al.*, *Nature* **465**, 901–904 (2010).
4. F. Jonietz *et al.*, *Science* **330**, 1648–1651 (2010).
5. X. Z. Yu *et al.*, *Nat. Mater.* **10**, 106–109 (2011).
6. S. Seki, X. Z. Yu, S. Ishiwata, Y. Tokura, *Science* **336**, 198–201 (2012).
7. H.-B. Braun, *Adv. Phys.* **61**, 1–116 (2012).
8. N. Nagaosa, Y. Tokura, *Nat. Nanotechnol.* **8**, 899–911 (2013).
9. S. Z. Lin, C. Reichhardt, C. D. Batista, A. Saxena, *Phys. Rev. Lett.* **110**, 207202 (2013).
10. J. Zang, M. Mostovoy, J. H. Han, N. Nagaosa, *Phys. Rev. Lett.* **107**, 136804 (2011).
11. M. Bode *et al.*, *Nature* **447**, 190–193 (2007).
12. S. Heinze *et al.*, *Nat. Phys.* **7**, 713–718 (2011).
13. A. Thiaville, S. Rohart, E. Jue, V. Cros, A. Fert, *Europhys. Lett.* **100**, 57002 (2012).
14. A. Fert, V. Cros, J. Sampaio, *Nat. Nanotechnol.* **8**, 152–156 (2013).
15. G. Chen *et al.*, *Nat. Commun.* **4**, 2671 (2013).
16. G. Chen *et al.*, *Phys. Rev. Lett.* **110**, 177204 (2013).
17. S. Emori, U. Bauer, S. M. Ahn, E. Martinez, G. S. Beach, *Nat. Mater.* **12**, 611–616 (2013).
18. S. Emori *et al.*, *Phys. Rev. B* **90**, 184427 (2014).
19. K. S. Ryu, L. Thomas, S. H. Yang, S. Parkin, *Nat. Nanotechnol.* **8**, 527–533 (2013).
20. O. Boulle *et al.*, *Phys. Rev. Lett.* **111**, 217203 (2013).
21. N. Perez *et al.*, *Appl. Phys. Lett.* **104**, 092403 (2014).
22. K. W. Kim, H. W. Lee, K. J. Lee, M. D. Stiles, *Phys. Rev. Lett.* **111**, 216601 (2013).
23. J. Sampaio, V. Cros, S. Rohart, A. Thiaville, A. Fert, *Nat. Nanotechnol.* **8**, 839–844 (2013).
24. S. Rohart, A. Thiaville, *Phys. Rev. B* **88**, 184422 (2013).
25. B. Dupé, M. Hoffmann, C. Paillard, S. Heinze, *Nat. Commun.* **5**, 4030 (2014).
26. A. Hoffmann, *IEEE Trans. Magn.* **49**, 5172–5193 (2013).
27. L. Liu *et al.*, *Science* **336**, 555–558 (2012).
28. A. V. Khvalkovskiy *et al.*, *Phys. Rev. B* **87**, 020402 (2013).
29. I. M. Miron *et al.*, *Nature* **476**, 189–193 (2011).
30. J. Iwasaki, M. Mochizuki, N. Nagaosa, *Nat. Nanotechnol.* **8**, 742–747 (2013).
31. Y. Tchoe, J. H. Han, *Phys. Rev. B* **85**, 174416 (2012).
32. Y. Zhou, M. Ezawa, *Nat. Commun.* **5**, 4652 (2014).
33. Supplementary materials are available on *Science* Online.
34. A. P. Malozemoff, J. C. Slonczewski, *Magnetic Domain Walls in Bubble Materials* (Academic Press, New York, 1979).
35. J. Eggers, *Rev. Mod. Phys.* **69**, 865–930 (1997).
36. R. Tomasello *et al.*, *Sci. Rep.* **4**, 6784 (2014).
37. G. Yu *et al.*, *Nat. Nanotechnol.* **9**, 548–554 (2014).
38. G. Q. Yu *et al.*, *Phys. Rev. B* **89**, 104421 (2014).
39. A. Hubert, R. Schafer, *Magnetic Domains: The Analysis of Magnetic Microstructures* (Springer, Berlin, Heidelberg, New York, 2008).
40. J. Choi *et al.*, *Phys. Rev. Lett.* **98**, 207205 (2007).
41. J. H. Franken, M. Herps, H. J. M. Swagten, B. Koopmans, *Sci. Rep.* **4**, 5248 (2014).
42. O. J. Lee *et al.*, *Phys. Rev. B* **89**, 024418 (2014).
43. N. Romming *et al.*, *Science* **341**, 636–639 (2013).
44. L. Sun *et al.*, *Phys. Rev. Lett.* **110**, 167201 (2013).
45. J. Li *et al.*, *Nat. Commun.* **5**, 4704 (2014).
46. B. F. Miao *et al.*, *Phys. Rev. B* **90**, 174411 (2014).
47. A. Hrabec *et al.*, *Phys. Rev. B* **90**, 020402(R) (2014).
48. S. S. P. Parkin, M. Hayashi, L. Thomas, *Science* **320**, 190–194 (2008).

ACKNOWLEDGMENTS

Work carried out at Argonne National Laboratory was supported by the U.S. Department of Energy (DOE), Office of Science, Materials Science and Engineering Division. Lithography was carried out at the Center for Nanoscale Materials, an Office of Science user facility, which is supported by the DOE, Office of Science, Basic Energy Sciences, under contract no. DE-AC02-06CH11357. Work performed at the University of California, Los Angeles, was partially supported by the NSF Nanosystems Engineering Research Center for Translational Applications of Nanoscale Multiferroic Systems. We thank I. Martin and I. Aronson for insightful discussion.

SUPPLEMENTARY MATERIALS

www.sciencemag.org/content/349/6245/283/suppl/DC1
Materials and Methods
Supplementary Text
Figs. S1 to S7
References
Movies S1 to S5

26 October 2014; accepted 28 May 2015
Published online 11 June 2015
10.1126/science.aaa1442

Blowing magnetic skyrmion bubbles
Wanjun Jiang *et al.*
Science **349**, 283 (2015);
DOI: 10.1126/science.aaa1442